

RESEARCH ARTICLE

10.1002/2014JD022821

Key Points:

- Wind turbines interact with the atmosphere and produce infrasound
- Wind-farm infrasound can propagate long distances
- Wind-farm infrasound could be used to probe the lower atmosphere

Correspondence to:

O. Marcillo,
omarcillo@lanl.gov

Citation:

Marcillo, O., S. Arrowsmith, P. Blom, and K. Jones (2015), On infrasound generated by wind farms and its propagation in low-altitude tropospheric waveguides, *J. Geophys. Res. Atmos.*, *120*, 9855–9868, doi:10.1002/2014JD022821.

Received 6 NOV 2014

Accepted 18 AUG 2015

Accepted article online 21 AUG 2015

Published online 3 OCT 2015

On infrasound generated by wind farms and its propagation in low-altitude tropospheric waveguides

Omar Marcillo¹, Stephen Arrowsmith², Philip Blom¹, and Kyle Jones²

¹Earth and Environmental Science, Los Alamos National Laboratory, Los Alamos, New Mexico, USA, ²Sandia National Laboratories, Albuquerque, New Mexico, USA

Abstract Infrasound from a 60-turbine wind farm was found to propagate to distances up to 90 km under nighttime atmospheric conditions. Four infrasound sensor arrays were deployed in central New Mexico in February 2014; three of these arrays captured infrasound from a large wind farm. The arrays were in a linear configuration oriented southeast with 13, 54, 90, and 126 km radial distances and azimuths of 166°, 119°, 113°, and 111° from the 60 1.6 MW turbine Red Mesa Wind Farm, Laguna Pueblo, New Mexico, USA. Peaks at a fundamental frequency slightly below 0.9 Hz and its harmonics characterize the spectrum of the detected infrasound. The generation of this signal is linked to the interaction of the blades, flow gradients, and the supporting tower. The production of wind-farm sound, its propagation, and detection at long distances can be related to the characteristics of the atmospheric boundary layer. First, under stable conditions, mostly occurring at night, winds are highly stratified, which enhances the production of thickness sound and the modulation of other higher-frequency wind turbine sounds. Second, nocturnal atmospheric conditions can create low-altitude waveguides (with altitudes on the order of hundreds of meters) allowing long-distance propagation. Third, night and early morning hours are characterized by reduced background atmospheric noise that enhances signal detectability. This work describes the characteristics of the infrasound from a quasi-continuous source with the potential for long-range propagation that could be used to monitor the lower part of the atmospheric boundary layer.

1. Introduction

Significant efforts have been made to study and characterize the sound from wind turbines (WTs) [Hubbard and Shepherd, 1991; Doolan *et al.*, 2012] as sound production may be linked to turbine performance and also as sound may annoy nearby residents [Møller and Pedersen, 2011; O'Neal *et al.*, 2011]. The study of wind-farm (WF) sound is especially important considering the increase in the number and size of WFs and individual turbines installed worldwide. Furthermore, there are concerns of the effect of large WFs on the dynamics of the atmosphere from local [Baidya Roy *et al.*, 2004] to global scales [Keith *et al.*, 2004; Kirk-Davidoff and Keith, 2008]. At local scales, the characterization of the interaction of the atmospheric boundary layer (ABL) flow with WTs has important implications for the design and operation of WFs [Porté-Agel *et al.*, 2014] with respect to energy conversion efficiency.

In terms of sound generation and propagation, the conditions of the atmosphere drive turbine's operation and determine sound propagation. WTs produce sound in the audible and infrasonic (<20 Hz) bands. Infrasound displays low atmospheric attenuation and dispersion and has the potential for long-range propagation, hundreds to thousands of kilometers [Drob *et al.*, 2003]. The propagation and detection of WF infrasound at large distances (tens of kilometers) require specific conditions to be met: (1) the infrasonic signal to be above background noise levels and (2) the formation of a waveguide to contain the infrasonic energy. This work starts by providing an overview of the operation of modern WTs, the generation of aerodynamic sound, and its interaction with the ABL.

1.1. Wind-Farm Sound and the Atmospheric Boundary Layer

1.1.1. Wind Turbine Operation

WTs capture kinetic energy from the atmospheric wind to produce electric energy. The central aerodynamic component of WTs is the rotor, which is composed of a hub and one or more blades. The blade length, the chord (line between leading and trailing edges), the pitch angle (angle between blade chord and the rotor

rotational plane), and the angle of attack (α , angle between the incoming wind and the chord) can describe the blade's geometry. WTs have different geometries (e.g., horizontal or vertical axes, one or more blades with different lengths, and different elevations for the rotor), operational configurations (e.g., fixed or variable rotor angular velocity (ω) and downwind or upwind facing blades), and control mechanisms (e.g., pitch and yaw controls), which are well summarized by *Arturo Soriano et al.* [2013].

Modern WTs have a horizontal axis with three blades oriented upwind and rotate at variable ω . By allowing the rotor to rotate at different speeds, depending on the incoming wind speed (w), the amount of extracted energy can be maximized as the efficiency of the energy conversion depends on the blade's tip speed ratio, $\lambda = v_{tip}/w$, where $v_{tip} = \omega r$ is the velocity of the blade's tip and r is the radius of the rotor [*Hau*, 2013]. Parameter ω can change but is kept within limits, which depend on the turbine characteristics and atmospheric conditions, to ensure the safety of the machinery. Parameter ω can be controlled by modifying the pitch angle [*Muljadi and Butterfield*, 2001]. Maximum, minimum, and rated wind speeds (w_{rmax} , w_{rmin} , and w_r , respectively) are defined for the operation of WTs with variable ω , which can operate in four different states: (1) if $w_{rmin} < w < w_r$, ω changes to maximize energy extraction; (2) if $w_r < w < w_{rmax}$, ω is kept at rated angular velocity (ω_r) by changing the pitch angle; (3) if $w < w_{rmin}$, ω may change but the turbine does not produce energy; and (4) if $w > w_{rmax}$ the pitch angle is modified to significantly slow or stop the rotation of the blades, the turbine does not produce energy. WTs are designed to operate at state 2 as long as possible so the rated output power is attained for the maximum amount of time.

1.1.2. Wind Turbine Sound

WTs produce mechanical and aerodynamic sounds that can be audible and/or infrasonic. Three atmosphere-turbine interactions are important for the generation of aerodynamic wind turbine sound: (1) blade and airflow gradients (thickness sound), (2) blade and inflow turbulence, and (3) turbulent boundary layer and trailing edge. *Hubbard and Shepherd* [1991] provide a comprehensive study of these interactions and show that radiation patterns for WF sound have typically the highest intensity in the upwind and downwind directions.

1.1.2.1. Thickness Sound

As a blade rotates it encounters flow gradients (e.g., the wake of the supporting tower for downwind rotors or low wind speed due to highly stratified wind profiles) that create abrupt changes in lift and drag that produce sound [*Hubbard and Shepherd*, 1991] (also known as thickness sound (TS) [*van den Berg*, 2005]). TS is characterized by energy peaks at the blade-passing frequency f_{TS} and its harmonics.

$$f_{TS} = N \frac{\omega}{2\pi}, \tag{1}$$

where N is the number of blades. As short pulses produce this type of sound, harmonics of this main frequency are usually observed. *Jung et al.* [2008] describe the observations of TS ($f_{TS} = 0.863$ Hz and $\omega = 1.806$ rad/s or 17.3 revolutions per minute (rpm)) from a 1.5 MW turbine at short distance (98 m) where up to the eighth harmonic was observed.

1.1.2.2. Inflow Turbulence Sound

The interaction of the turbine blades with turbulence embedded in the airflow produces rapid changes in the blade load that creates sound. The presence of this type of noise depends on the relative size of the turbulence compare to the blade, and it is nonperiodic. This type of sound has broadband spectrum with peak amplitude at [*Grosveld*, 1985]

$$f_{IF} = \frac{St0.7r\omega}{H - 0.7r}, \tag{2}$$

where H is the turbine height, r is the blade length, and St ($=16.6$) is the Strouhal number. *Hubbard and Shepherd* [1990] show complete frequency spectra for inflow turbulence sound for WTs with different blade lengths recorded few hundreds of meters from the source.

1.1.2.3. Trailing Edge Sound

The turbulent boundary layer on the surface of a blade generates pressure fluctuations that are scattered by the trailing edge and produce broadband sound. The energy for this broadband sound is centered above the infrasound band and accounts for most of the audible energy radiated by modern WTs

[Wolf *et al.*, 2014]. As the frequencies for this type of sound are higher than the other types its absorption in the atmosphere is higher and its propagation limited to short distances. The trailing edge sound is centered at [Moriarty and Migliore, 2003]

$$f_{TE} = \frac{0.02r\omega}{\delta^* M^{0.6}}, \quad (3)$$

where M is the Mach number and $\delta^* = \delta^*(Re, C, \alpha)$ is the displacement thickness, which depends on the Reynolds number (Re), the chord length (C), and α and is used to measure the thickness of the boundary layer [Schlichting and Gersten, 2000]. Oerlemans *et al.* [2007] characterized and located trailing edge sound from an 850 kW turbine sound with frequencies between 0.6 and 1 kHz. The trailing edge sound can be amplitude modulated [Larsson and Ohlund, 2014] at the blade-passing frequency [Doolan *et al.*, 2012]. The sudden changes in the angle of attack [van den Berg, 2005] and the downward movement of the blades [Oerlemans and Schepers, 2009] have been proposed as potential mechanisms for this modulation.

1.1.3. The Atmospheric Boundary Layer and the Propagation of the Sound From Wind Turbines

The atmospheric boundary layer (ABL) is defined as the lower part of the troposphere, where the interaction of the ground and the atmosphere occurs. The ABL fluctuates in height and can extend from tens of meters to a few kilometers. Three different ABL regimes can be distinguished [Emeis, 2010]: (1) convective boundary layer (CBL) if thermal convection dominates (usually daytime conditions), (2) stable boundary layer (SBL) if the atmosphere cools from below (usually clear nighttime conditions), and (3) neutral or dynamical boundary layer if shear forces dominate under no heat flux conditions (cloudy conditions).

The ABL provides very different conditions for the operation of WTs and for the generation and propagation of sound. For example, the SBL provides for larger-energy potential due to strong shear and low turbulence. These are also favorable conditions for long-range propagation; for example, van den Berg [2004] reported on sounds being more noticeable due to low background noise and more favorable conditions for turbine operation at night. The CBL is characterized by a more turbulent regime, with lower degree of wind stratification, and a characteristic thermal profile in which temperatures decrease away from the ground resulting in upward refraction of sound.

To relate the atmospheric parameters to sound propagation we define the effective sound speed, $c_{eff}(z) = \sqrt{\gamma R \sqrt{T(z)} + w(z) \cdot n}$, where $\gamma = 1.4$ is the ratio of specific heats, $R = 287$ is the gas constant, z is the elevation, T is the air temperature, w is the wind, and n is the vector normal to the wavefront [Garcés *et al.*, 1998]. For downward refracting atmospheric conditions that form acoustic waveguides, we define the maximum height of the waveguide (h_{max}), as the elevation with the maximum c_{eff} and the launch angle of the critical ray (the raypath for which the turning height is h_{max}), $\theta_{crit} = \cos^{-1}(c_{eff}(0)/c_{eff}(h_{max}))$ [Jensen *et al.*, 2011]. Assuming a no-slip boundary condition, the wind at the ground vanishes, and $c_{eff}(0)$ is approximately the adiabatic sound speed at the ground.

Certain configurations of the ABL can lead to the creation of tropospheric low-altitude acoustic waveguides. Long-distance propagation of sound in the lower atmosphere under SBL conditions has been significantly studied [Talmadge *et al.*, 2008; Waxler *et al.*, 2008]. For example, Fee and Garcés [2007] recorded volcanic infrasonic tremor at 12 km from the source and attributed to energy ducted in a SBL waveguide. Herrin *et al.* [2006] described infrasound signals from impulsive sources with estimated distance to the source of 102.7 km and modeled a low-altitude waveguide formed by warm air moving above the ocean surface; Johansson [2003] also modeled low-level jets to study noise from offshore WFs. These studies have modeled and observed waveguides due to inversions with elevations of the order of a few hundreds of meters. Other sections of the troposphere above the ABL can introduce wind features (e.g., the jet stream at 10–12 km) that can create acoustic waveguides [Drob *et al.*, 2003]. Such features are not necessarily related to local heat transfer of the ABL, although they are important to include when considering long-distance propagation of infrasound in the troposphere.

2. Data and Methods

2.1. Experiment Setting and Data

This deployment comprised four arrays, i.e., LAG (Laguna), MOT (Motor), SNL (FACT-Site array, Sandia National Laboratories), and LISA in a linear configuration oriented southeast at 13, 54, 90, and 126 km radial distances and

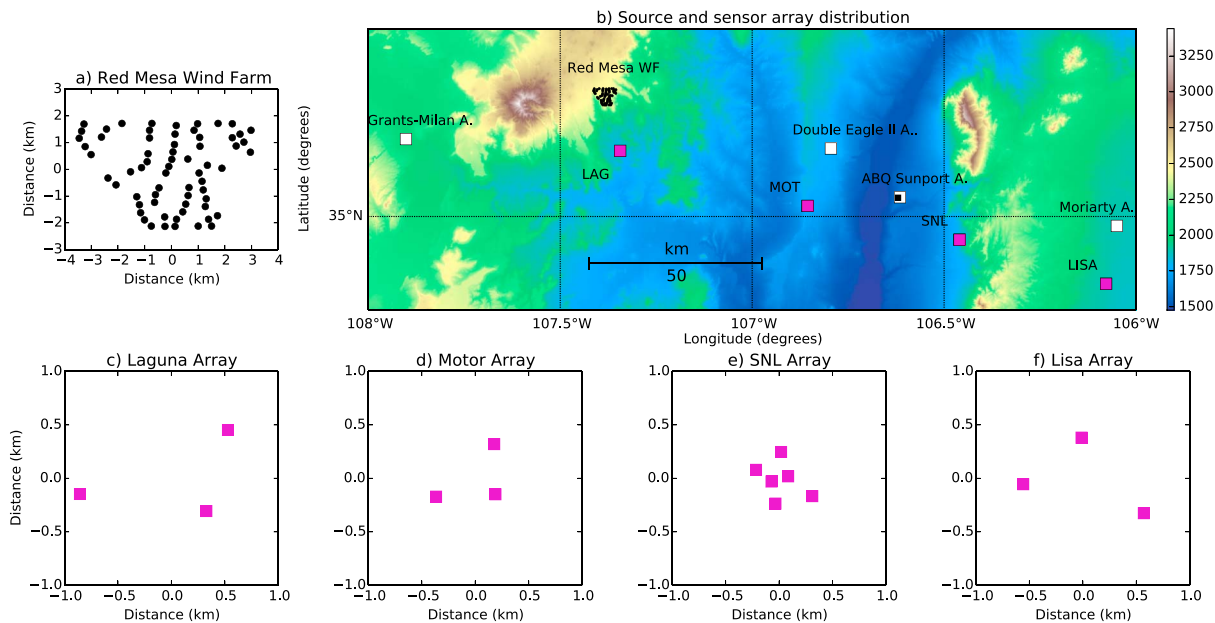


Figure 1. (a) Distribution of the turbines (black dots) in the RMWF. (b) Topographic map with the locations of the sensor arrays (magenta squares), the available weather stations (white squares), and radiosonde launch site (small black square). (c–f) Array geometries.

azimuths of 166°, 119°, 113°, and 111° from the Red Mesa Wind Farm (RMWF), Laguna Pueblo, New Mexico, USA (Figure 1). The sensor arrays were configured with apertures of 0.6, 0.5, 0.9, and 0.6 km, respectively. LAG, MOT, and LISA arrays had three and SNL six sensors. The array nodes comprised Hyperion (model IFS-3000) and Chaparral (model 2.5) sensors with 15 m porous hoses. These two types of sensors featured flat responses (within 3 dB) in the 0.1 to 100 Hz band and self noises below 5 MPa.

The RMWF site comprises 60 GE 1.6–82.5 turbines [Diffendorfer et al., 2014] which belong to the General Electric 1.6 MW turbine family and have a horizontal axis with three blades and active yaw control for upwind operation, variable rotor angular velocity, and pitch control. These turbines are rated to $w_r = 12$ m/s, $w_{rmin} = 4$ m/s, and $w_{rmax} = 25$ m/s [Pennock, 2012]. With λ between 6 and 8 (these values maximize the power conversion for this type of turbines for low pitch angles; see Figure 4.11 in Clark et al. [2010]) and w_r , the rotor speed is estimated between 16.6 and 22.2 rpm. Table 1 shows a summary of rated and estimated parameters for the turbines at the RMWF.

Figure 2 shows examples of the collected waveforms and their corresponding spectrograms for periods with low atmospheric background noise. The pressure is shown in pascals (Pa) and the units of the spectrograms in dB/Hz relative to 20 μ Pa. Figures 2a–2c correspond to observations at LAG, MOT, and SNL (respectively) on 4 February 2014, 4:00 UTC. These spectrograms, constructed using window lengths of 60 s with 50% overlap,

show sharp peaks with fundamental frequency slightly below 0.9 Hz and its harmonic. We located these peaks more precisely at 0.879 Hz and multiple integers of this frequency by analyzing the energy spectrum of longer window lengths (480 s) that allow for higher-frequency resolution. We use 0.879 Hz as the fundamental TS frequency for all analysis in this manuscript. The fundamental frequency and the first four harmonics are shown in the figure, but up to a seventh harmonic can be

Parameter	Value	Unit
Turbine power	1.6	MW
Turbine total height	121	m
Tower type	Monopole	not applicable
Tower/hub height	80	m
Blade length	41.25	m
Rotor diameter	82.5	m
Cut-in wind speed	3	m/s
Cut-in high wind velocity	25	m/s
Rated wind velocity	12	m/s
Estimated rotor speed ($\lambda = 6$)	16.6	rpm
Estimated rotor speed ($\lambda = 8$)	22.2	rpm

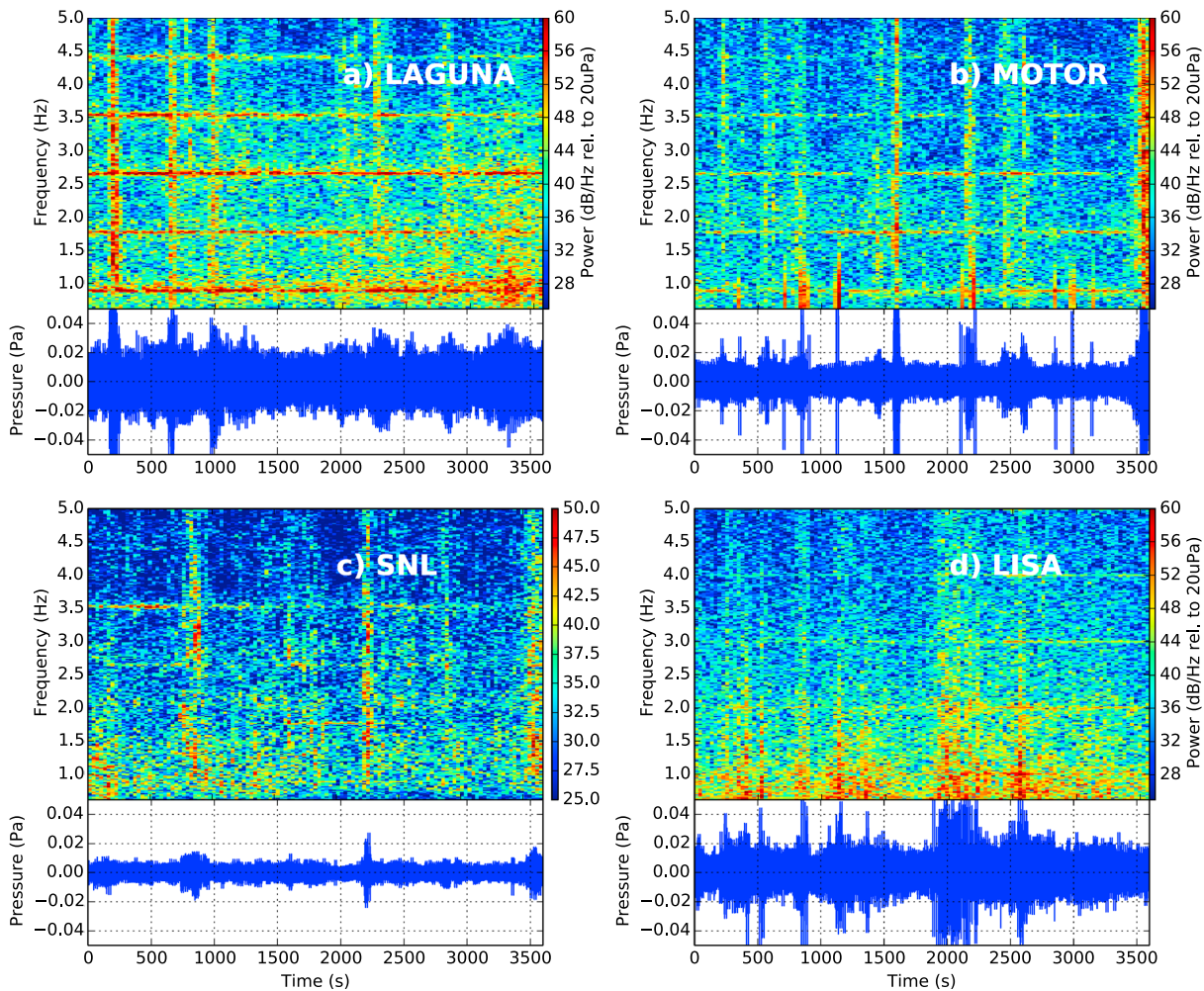


Figure 2. Example of waveforms and their spectrograms. The waveforms show the best beams (see section 2.2 for details of the calculation) and were filtered between 0.6 and 10 Hz with a four-pole zero-phase filter. The spectrograms were constructed with 60 s windows with 50% overlap. (a–c) 4 February 2014 at 04:00 UTC. These spectrograms show energy peaks at a frequency slightly below 0.9 Hz and its harmonics. Note that SNL spectrogram has a slightly shorter color map; this was used to enhance the visibility of the WF sound bands. For the same period the LISA array had high noise levels and it is not shown. (d) 17 February 11:00 UTC; note the energy peaks at around 1 Hz and its harmonics.

distinguished at the LAG and MOT arrays and up to a third harmonic for SNL. Note that the attenuation of the waveforms as the distance from the WF to the receiver increases. The waveform for the LISA array for this period shows very high background noise levels, and it is not shown. Figure 2d corresponds to observations at LISA array on 17 February 2014, 11:00 UTC. The LISA array displays energy peaks with central frequency around 1 Hz and its harmonics. Local climatological data, i.e., radiosonde measurements and local weather stations, are also available for the area. The radiosonde profiles correspond to station 72,365 located in Albuquerque, NM (data available at the repository of the Department of Atmospheric Science of the University of Wyoming). These soundings are performed twice a day at 00:00 and 12:00 UTC, 17:00 and 05:00 local standard time (LST). Quality-Controlled Local Climatological Data from the NOAA National Climatological Data Center for four stations are available in the area: (1) Grants-Milan Municipal airport (ID:93057), (2) Double Eagle II airport (ID:03034), (3) Albuquerque International Sunport airport (ID:23050), and (4) Moriarty airport (ID:03033). Figure 3 shows a summary of the winds for the month of February 2014 for the four stations with plots separated by day (07:00 A.M.–07:00 P.M.) and night hours (07:00 P.M.–07:00 A.M.).

2.2. Detection and Characterization of WF Sound

Data from a sensor array can be used to estimate the horizontal velocity (trace velocity, \vec{v}_{tr}) of a signal as it propagates across the array. Beamforming is an array-processing technique for the estimation of \vec{v}_{tr} ; this

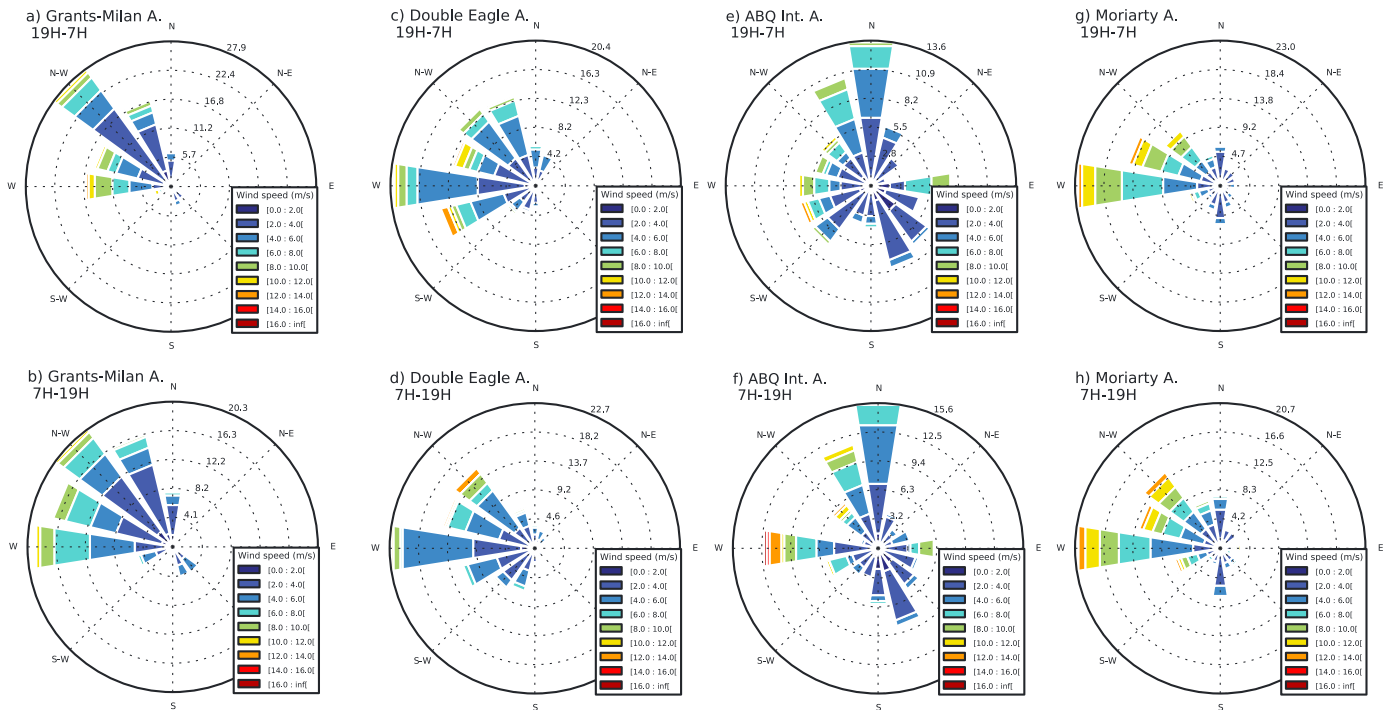


Figure 3. Wind measurements from local weather stations. The subplots show wind rose plots for February 2014 for the four weather stations around our experiment area. The plots are divided by daytime and nighttime hours of the local time, wind speed is color coded, and the radial axis has been normalized to the percentage of the wind at specific azimuthal bins. The azimuths for the wind roses are divided in 16 sectors of 22.5°.

technique is based on time shifting the waveforms from the array assuming that the signal propagates with a specific \vec{v}_{tr} , averaging the shifted waveforms to form a beam, and finding the trace velocity that maximizes the beam power [Schweitzer *et al.*, 2002]. The beam that maximizes the power is called the best beam. We use the frequency-wave number (f-k) method [Thomas, 2008] to process the array data. This method operates in the frequency domain by shifting the phase of the signals (as this corresponds to time shifts in the time domain). With at least three sensors in an array, \vec{v}_{tr} can be determined (magnitude and direction (i.e., azimuth or back azimuth)). The relative power (a dimensionless value between 0 and 1) can also be defined as the ratio of the power of the best beam and the average power of the individual sensors. The relative power provides information about the coherency of the signal between the different waveforms. For our data analysis, we filtered the data with a four-pole, zero-phase band-pass filter between 0.7 and 2 Hz. This band includes the fundamental and first harmonic. For the f-k analysis we use a 480 s window with 50% overlap, and the search for the best beam is performed on the same 0.7 to 2 Hz band. We tested different window lengths, between 30 and 480 s, and found reduced aliasing on larger windows.

We analyze the energy spectrum of the 480 s best beams to detect the presence of signals with WF sound exhibiting TS characteristics (a fundamental peak with harmonics). We start by computing the power spectral density (PSD) of the best beams, which come from the f-k analysis described previously. The 0.7–2 Hz section of the PSD shows a trend with increasing energy for low frequencies, which is removed (detrended) in order to compute the standard deviation (σ_d). As we have identified the TS frequency at 0.879 Hz, we look for this peak in each detrended PSD. If the energy at the detrended PSD at 0.879 Hz is bigger than $2\sigma_d$ we consider this section to contain WF sound. This analysis uses the $2\sigma_d$ criterion to provide a 95% confidence in the detection.

2.3. Modeling Acoustic Propagation

To model the propagation of sound from the RMWF we use the parabolic equation (PE) method along with radiosonde measurements. The PE method provides an efficient means to compute the propagation of acoustic energy from a monopole source in an atmosphere with variable temperature and wind under the

condition that propagation is dominantly horizontal. The method consists of separating the wave equation into outward and inward propagating radial components and using the outward propagating “one-way wave equation” solution to numerically determine the refraction of the acoustic energy as it propagates away from the source. For a more detailed discussion of parabolic equation methods, see *Salomons* [2001] and *Jensen et al.* [2011]. We use an implementation of the PE method developed by *Assink* [2012], which is part of the ncaprop infrasound propagation software package [*National Center of Physical Acoustics*, 2012].

3. Results

3.1. Detection and Characterization of WF Sound

For the study period (February 2014), WF sound with TS characteristics was detected in 9.4%, 3.1%, and 0.9% (for LAG, MOT, and SNL, respectively) of the 28 days analyzed. Of these detections 80%, 85%, and 61% occurred at nighttime hours. Figure 4 shows the results for the detection of WF sound and the corresponding f-k processing results. Figures 4a–4f show the average of the PSDs of the best beams for all the segments with and without detections organized by daytime (A.M.) and nighttime (P.M.) hours. The mean energy at 0.879 Hz for the intervals with detections for the daytime (nighttime) hours are 57 dB (57 dB), 61 dB (53 dB), and 54 dB (48 dB) for LAG, MOT, and SNL, respectively. Note that the background level for the averaged spectrum for MOT array is consistently a few decibels above those for LAG even though they used the same type of noise reduction system and number of sensors. This may be due to the MOT array being located in a noisier environment, as it was deployed few hundreds of meters from U.S. Interstate 25. The SNL array shows PSDs with significant lower noise across all frequencies for detection and nondetection periods. This is likely due to the higher number of elements in the array and a quieter site. The detection algorithm applied to LISA array shows fewer detections with no particular preferential back azimuths. Spectral analysis on the signal of the LISA array shows other peaks, e.g., around 1 Hz, that may be related to other wind farms in the area, e.g., the Aragonne (back azimuth and radial distance to LISA array: 92°, 93 km, respectively), Juan (115°, 230 km), or Lone Some (166°, 44 km), which feature different turbines and may operate at different angular velocities.

The f-k results for the segments with detected WF sound show back azimuths with the most frequently occurring values (or modes) of 348°, 299°, and 295°, for LAG, MOT, and SNL arrays, respectively. These results show 2°, 0°, and 2° difference to the geometrical back azimuth (346°, 299°, and 293°) of the center of each array to the mean location of the RMWF. Most of the trace velocities have magnitudes between 340 and 355 m/s, corresponding to very shallow propagation angles. Figures 4g–4i show the results of the f-k analysis. The histograms for the back azimuths, displayed in polar plots, are grouped in bins with 4° width. The bins with the most frequent back azimuths correspond to 344°–348° for LAG, 296°–300° for MOT, and 292°–296° for SNL (we called these back azimuth regions the back azimuth principal components). As the histogram for SNL shows two back azimuth bins, 288°–292° and 292°–296°, with significant number of detections, we consider both regions as the principal component of the SNL histogram. Figures 4j–4l show histograms of the detections with the corresponding hours (local time) of the detections. Note the significant reduction in the number of daytime detections, especially for LAG and MOT arrays, which agrees with an increase in signal detectability at nighttime hours [*Fee and Garcés*, 2007; *Talmadge et al.*, 2008].

3.2. The ABL and the Long-Distance Propagation of Wind-Farm Sound

Figure 5 shows the results of the back azimuths of the WF sound detections along with relative effective sound speed (assuming a propagation vector from RMWF to SNL array) profiles from radiosonde data. We divided the profiles in daytime and nighttime hours (Figures 5a and 5d, respectively) and evaluated the existence of waveguides in each profile and estimated h_{\max} (Figures 5b and 5e) and θ_{crit} (Figures 5c and 5f). We also show the distribution in time of the back azimuths of the principal components for each array. Figure 5 shows that some of the profiles have waveguide characteristics (i.e., relative $c_{\text{eff}}(z)$ that increases with elevation), mostly occurring at nighttime, that coincide with an increased number of detections with back azimuths corresponding to the RMWF (see days 14–18).

3.2.1. Modeling the Propagation Waveguide

Below, we analyze radiosonde data and use propagation modeling to explain some of the characteristics of the propagation of WF sound with TS characteristics. As radiosonde measurements are taken daily at 05:00 A.M. and 05:00 P.M., local time, at the Albuquerque station, the profiles represent two different atmospheric scenarios (respectively): (1) atmospheric conditions at the end of the nighttime hours with SBL features and (2) conditions

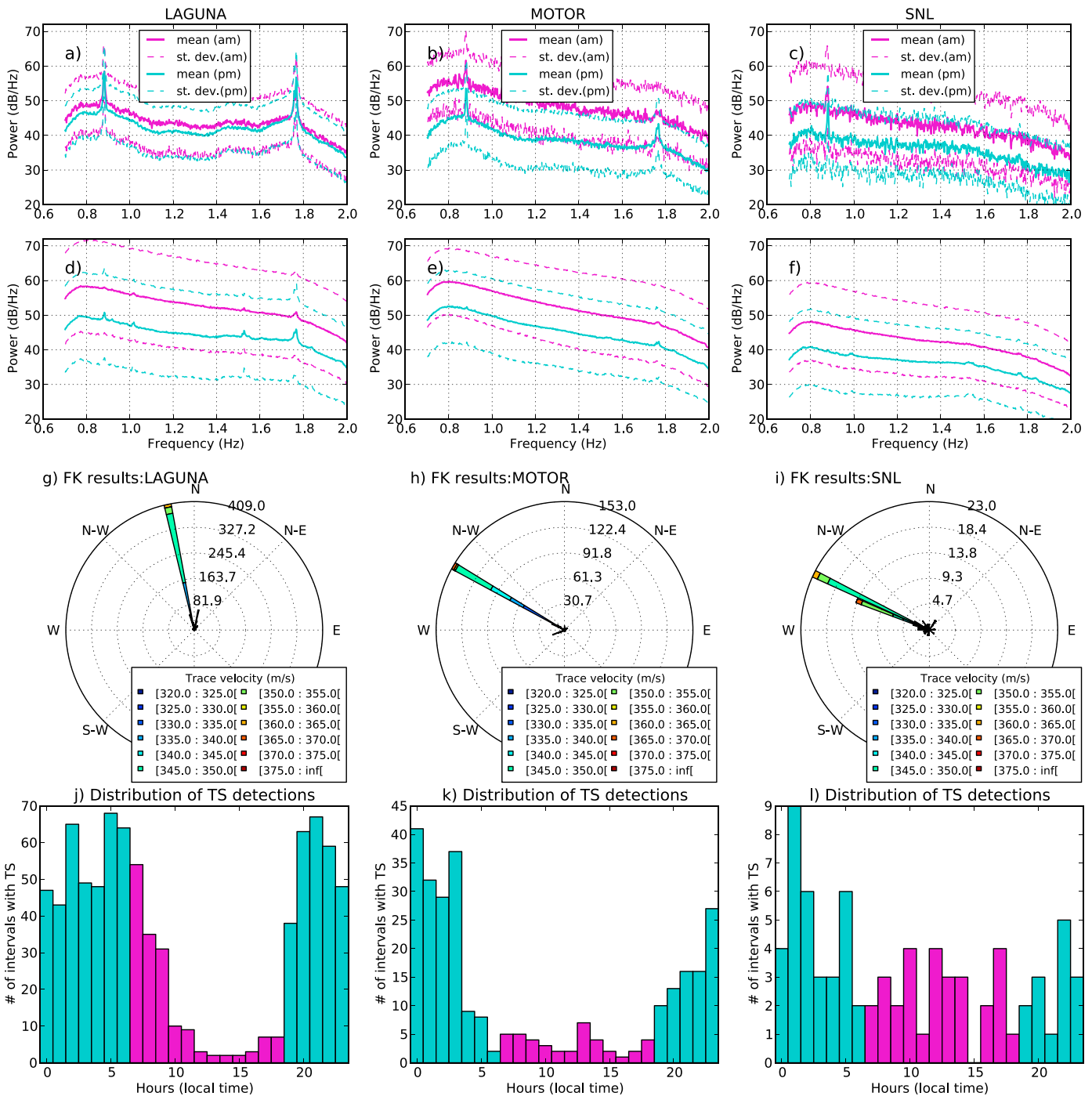


Figure 4. WF sound detection and array-processing results. PSDs for sections with and without TS peaks detected for (a and d) LAG, (b and e) MOT, and (c and f) SNL arrays separated by day and night LST hours (magenta and cyan, respectively). (g–i) Results of the f-k analysis (for intervals with WF sound detection) with back azimuths in polar plot histograms color coded with the magnitude of trace velocity (histogram’s bin width = 4°). (j–l) The distribution of the detections with hours of the LST also color coded according to day and night hours (magenta and cyan, respectively).

at the end of the daytime hours with CBL features. By using these two daily profiles we gain some insight of the propagation under different atmosphere scenarios for the fundamental frequency of the TS and its harmonics.

The PE method allows one to determine transmission loss (TL) as a function of frequency, which is of particular interest here due to the limited thickness of the boundary layer and the large wavelengths corresponding to the described WF sound. As the radiosonde profiles do not indicate a strong jet stream at 10 km we expect

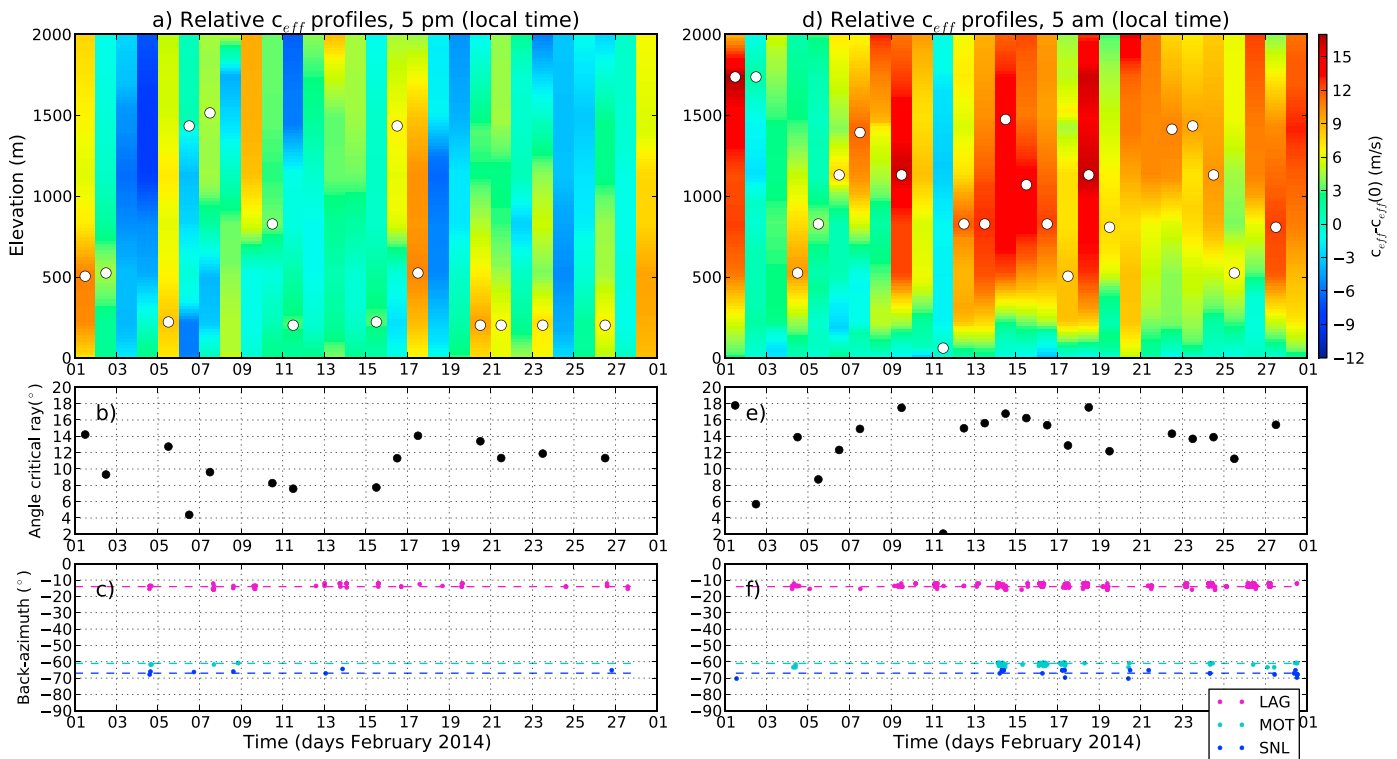


Figure 5. (a and d) Relative effective sound speed profiles for daytime and nighttime hours, respectively (white dots correspond to h_{max}). (b and e) Corresponding θ_{crit} for h_{max} . (c and f) Distribution in time of back azimuths obtained by f-k analysis; only the back azimuths within LAG: -12° to -16° , MOT: -60° to -64° , and SNL: -64° to -72° are shown, which correspond to the principal components of the histograms shown in Figures 4g–4i. The dashed colored lines show the geometrical back azimuths.

ducting to occur at lower altitudes. Figure 6 shows radiosonde measurements (for the lowest 2 km) for 17 February (05:00 P.M.) and 18 February (05:00 A.M.) 2014 (local time) in Figures 6a and 6d, respectively, and the corresponding TL maps obtained by the application of PE method to fundamental and first harmonic frequencies. These two profiles show typical CBL and SBL conditions. For the 05:00 P.M. profile, the effective sound speed decreases with altitude in the first 1000 m and sound refracts upward. In such a case there is no waveguide in the lowest 2 km of the atmosphere. Figures 6b and 6c show TL maps for range and elevation of the fundamental and first harmonic frequencies, respectively.

The ducts, with specific characteristics to each frequency, formed by the SBL conditions (Figures 6e and 6f) have vertical extents between 500 and 700 m for the fundamental frequency and between 300 and 400 m for the first harmonic (leakage above these channels extends few hundreds of meters). Comparing radiosonde data for the duration of this experiment, it has been found that h_{max} of the waveguide in the morning hours varies between 200 and 1500 m. The height of the waveguide and the wavelength of WF sound determine the efficiency of the propagation. The wavelengths corresponding to the fundamental frequency and the first two harmonics of RMWF's TS are 390, 195, and 97.5 m (assuming a 343 m/s sound speed). Figure 7 shows the PE prediction for TL at the ground for various propagation ranges using the different frequency components of the TS (Figure 7a) and the same prediction for multiple azimuths (Figures 7b–7e). The results shown in Figure 7a are for an azimuth of 113° with respect to the wind farm. Using the 05:00 A.M. profile to represent typical SBL propagation, the amplitudes of the TS' harmonics are expected to be 3 to 5 dB louder than the fundamental. It should be noted that this prediction is unique to the atmosphere specifications obtained from the radiosonde on the morning of 18 February.

4. Discussion

The continuous infrasound recorded for the three closest arrays in this experiment show periods with the spectral characteristics of WT's TS with discrete energy peaks at 0.879 Hz and its harmonics. The results of

a) Sound speed prof. 5 pm

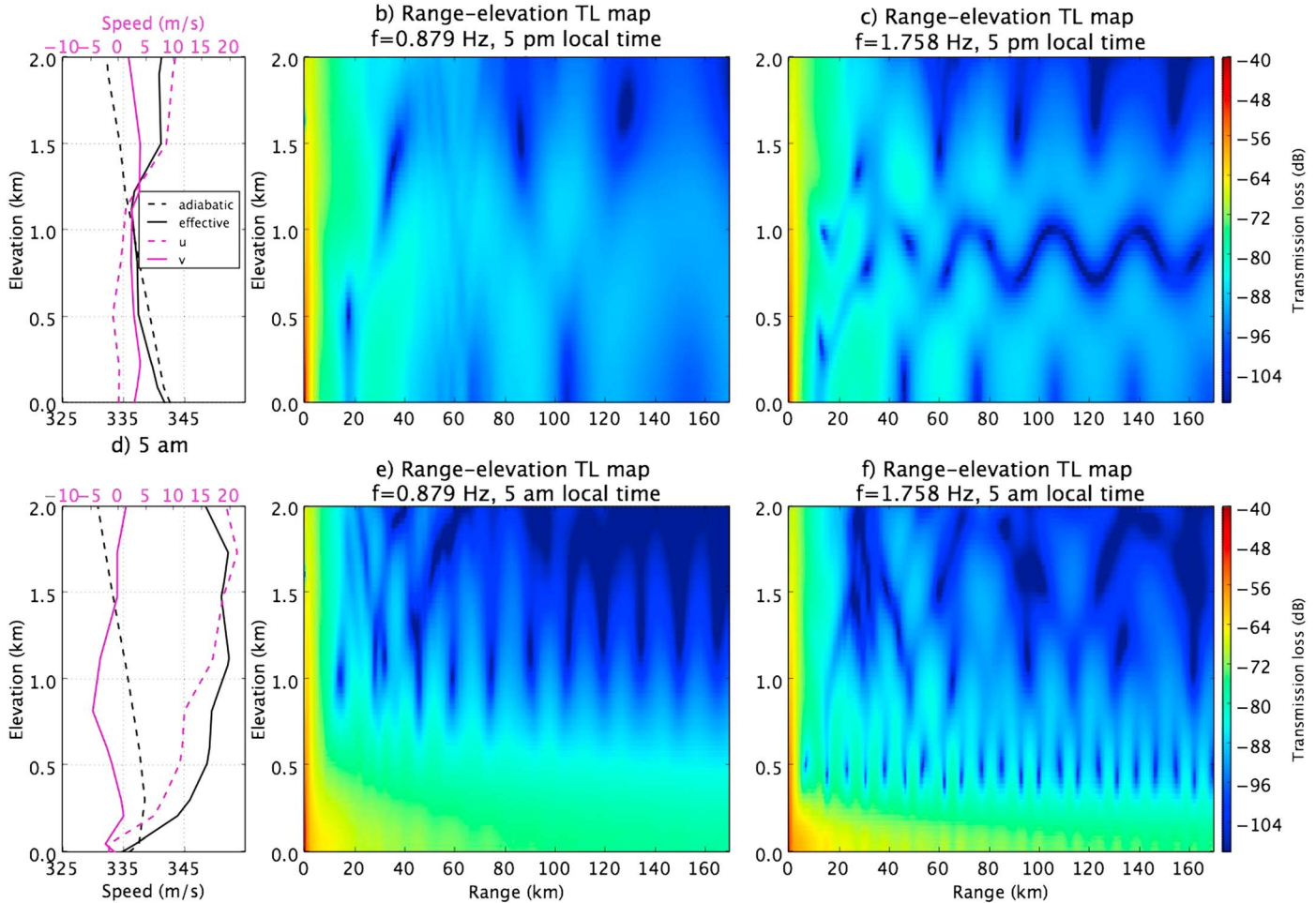


Figure 6. (a and d) Adiabatic and effective sound speeds (dashed and solid black lines) and zonal (u) and meridional (v) wind component (dashed and solid magenta lines) profiles for the Albuquerque radiosonde data corresponding to 17 and 18 February at 05:00 P.M. and 05:00 A.M., respectively (LST). (b, c, e, and f) Range-elevation transmission loss (TL) maps for the fundamental and first harmonic frequencies.

the array processing for the three closest arrays confirmed that periods with WF sound have back azimuths corresponding to the RMWF. Also, the local meteorological data (Figure 3) show prevailing winds in the experiment area that could favor the propagation of the RMWF's sound to our sensor arrays. As the actual operational parameters of the RMWF's WTs are not publicly available, we cannot corroborate that the spectral characteristics of the observed signal correspond to the actual operation parameters of the WTs. However, using equation (1) and the publicly available information [Diffendorfer *et al.*, 2014], we determined $\omega = 17.58$ rpm, which is within the range of ω_r for the RMWF's WTs (Table 1). We cannot distinguish with the present instrumentation if the signal is TS and/or amplitude modulation of other high-frequency WT-sound types (with sufficiently low frequency to support long-distance propagation) with similar spectral characteristics (peaks at the blade-passing frequency). Previous studies [Willshire, 1985; Son *et al.*, 2010; Ohlund and Larsson, 2015] have reported and modeled the propagation of WT sound to distances from few hundreds of meters to several kilometers. This study shows that WT noise can be detected at distances of several tens of kilometers.

The array analysis of the WF sound described here is challenging as the signal is tonal and narrow frequency bands required for the analysis is prone to aliasing. We found that a broader frequency band reduces the aliasing as more than one of the energy components are included in the f-k analysis. We are using the 0.7 to 2 Hz band to include the fundamental frequency and the first harmonic (which are the ones that are

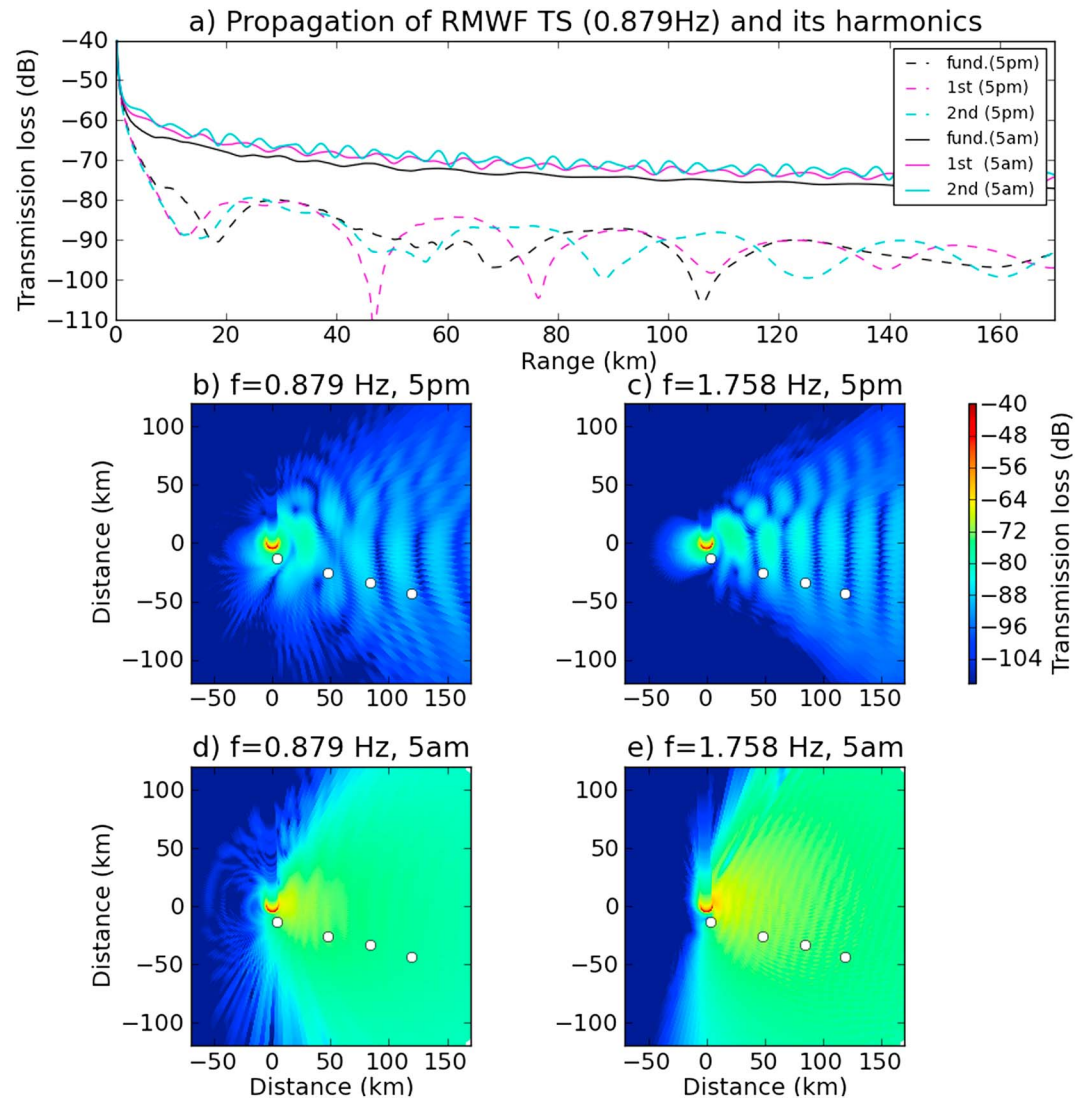


Figure 7. (a) TL profile at the ground for an azimuth of 113° , for the fundamental frequency (black), first (magenta), and second (cyan) harmonics; the radiosonde measurements correspond to those described in Figures 6a and 6d. TL (color-coded) at the ground for different ranges and azimuths for the fundamental frequency and first harmonic are shown for the (b and c) 05:00 P.M. and (d and e) 05:00 A.M. profiles. The location of the arrays (white dots) used in this experiment is shown relative to the wind farm.

present in most of the intervals with WF sound detection). This strategy yielded good results for the LAG and MOT arrays as the signal is strong and there are not highly populated areas that can contaminate the frequency band continuously. For the SNL array, the TS peak is small (as the signal has travelled around 90 km) and can easily be masked by background noise and the close proximity of the city of Albuquerque introduced continuous noise that may have affected WF sound detection (see detection at SNL is below 1%) and the estimated back azimuths from the array processing. We also tested the f-k analysis with different window lengths, between 30 and 480 s, and found reduced aliasing on larger windows. We are exploring the utilization of other filtering schemes (e.g., comb filters [Nishi and Ando, 1998]) to track instantaneous changes in peak frequency [Nehorai and Porat, 1986] and reduce the influence of persistent sources of noise to enhance the array processing. Also, the $2\sigma_d$ rule we use for the detection algorithm could be revised to find a number of σ_d that optimizes the detection algorithm.

We focused our analysis on the WF sound with discrete low-frequency peaks observed in our sensor arrays. However, the expected inflow turbulence sound for the RMWF is also in the infrasonic band ($f_{IF} = 17.12$ Hz,

using $\omega = 17.58$ rpm) and has also the potential for propagation at tens of kilometers. As inflow turbulence sound features a broadband spectrum and wavelengths in the order of few tens of meters (19.51 m assuming a 343 m/s sound speed propagation), waveguides with h_{\max} of few hundreds of meters (like the ones found in this study; see Figure 5) may efficiently duct this type of sound. Further research could explore the inflow turbulence sound to constrain the details of the waveguide and even the potential for signal dispersion.

We found that wind-farm sound propagated at least 90 km (reaching the SNL array) with radiosonde profiles showing the presence of low-altitude waveguides. These profiles show h_{\max} for the waveguides between 200 and 1800 m with the potential to refract rays with θ_{crit} up to 18° (Figure 5). We found that profiles with strong ducts (high θ_{crit}) are correlated with an increased number of detections especially at SNL array, see days 14–18 in Figure 5c. There are, however, periods with strong ducts (days 22 and 23) without detections at any of the arrays. This may imply that our assumption that the Albuquerque radiosonde profiles are representative of the atmosphere in our study area does not hold all the time and significant horizontal heterogeneities may be present. Furthermore, radiosonde profiles are only snapshots of the atmosphere at a specific space and time. As wind and temperature can change rapidly and radiosonde measurements are taken only every 12 h, atmospheric configurations that favor sound propagation (lasting several hours) may not be captured by the radiosonde. Regarding the LISA array (located 126 km from RMWF), the results of its f-k analysis and detection algorithm did not show sound with preferential back azimuths corresponding to the RMWF. We suspect that the Sandia Mountain range may distort the waveguide and prevent the signal from propagating beyond the mountain range.

The propagation of WF sound at different azimuths is also an important aspect in source and propagation characterization that we are addressing with propagation modeling (Figure 7). WF sound-recorded upwind and downwind are likely to have very different amplitudes [Hubbard and Shepherd, 1991]. In order to assess the variation in propagation effects with azimuth, we have modeled the expected amplitude at different ranges and azimuths using daytime- and nighttime-type profiles. Figures 7b–7e show that the sensor arrays described in this work were deployed within the ensonified region where the waveguide carries sound preferentially during both the day and night. Thus, for the case of WF sound in the infrasonic band, like the one studied here, it is expected that the signal will travel long distances preferentially in the direction of prevailing winds (see Figure 3). However, within 25–50 km of the source, sound with significant amplitude is expected at almost all azimuths. Note also that the TL maps in Figure 7 show that the acoustic energy is better confined for the first harmonic compared to the fundamental frequency; this is again likely due to the finite thickness of the waveguide.

The infrasonic signal observed at some distant location due to the WF is a result of the combined contributions from individual WTs distributed in space. For thickness sound, a WT generates a signal displaying short pulses repeating at the f_{TS} that are seen in the frequency spectrum as peaks at the f_{TS} and its harmonics. We denote this signal at one receiver as $p(t)$ and let $S(f) = |P(f)|^2$ be the energy spectral density of $p(t)$, where $P(f)$ is the Fourier transform of $p(t)$. $S(f)$ contains peaks at the f_{TS} and its harmonics. For a WF as whole, the pulses from different WTs (assuming that they operate at the same ω_r and thus have the same f_{TS}) arrive at the receiver with a relative phase delay dependent on the relative phase of the rotation of the blades of each WT, the geometry of each source-receiver pair, and the travel time along the propagation path. Assuming that the signals from different WTs arrive at the receiver with approximately equal amplitude, we can write each contribution as $p_n(t) = p(t - t_n)$ and the corresponding Fourier transform $P_n(f) = e^{-i2\pi f t_n} P(f)$, where t_n is the relative phase delay of the n th turbine. For a WF with M WTs, the resulting signal, $p_T(t)$, at the receiver is $p_T(t) = \sum_{k=1}^M p_k(t - t_k)$ and the energy spectral density then has the form

$$S_T(f) = |P_T(f)|^2 = |P(f)|^2 \left| \sum_{k=1}^M e^{-i2\pi f t_k} \right|^2. \quad (4)$$

Equation (4) shows that the combined signal from multiple WTs (generating TS with the same f_{TS}) will display TS spectral characteristics. Note that equation (4) is bounded as $S_T(f) \leq |P(f)|^2 M^2$, where the upper bound of the inequality holds in the unlikely scenario that all pulses arrive at the receiver with 0 relative phase delays. For more realistic scenarios t_n should be considered a random variable. Further research could explore the

construction of a more general equation (4) (e.g., pulses with different amplitudes and slightly different f_{TS}) and its estimation for WFs with a large number of turbines.

We have described and analyzed the characteristics of a quasi-continuous source of infrasound with the potential for propagation at distances in the order of several tens of kilometers. As WFs become larger, WTs also increase in size, shifting their aerodynamic noise to lower frequencies. This additional source of low-frequency background noise may affect the detection and location capabilities for infrasound arrays sitting near large WF deployments. For example, I57US (Pinon Flat, CA) is an installation of the International Monitoring System that sits approximately 35 km from a large wind-farm development (San Gorgonio Pass Site). It is possible that the sound from this wind park limits the detection capabilities of the array, especially for low-amplitude signals. However, with the proper characterization of the WF sound, and its propagation, its effects on infrasound records can be reduced. As the location of the source is known and the WF sound can be well characterized, the sound from wind farms can also be used to test the capabilities of infrasound instrumentation under a persistent signal. For example, WF sound could be used to assess detection capabilities of a sensor array or test spatial wind reduction filters with a persistent source under different atmospheric conditions.

5. Conclusions

We found that under specific atmospheric conditions, especially during the nighttime hours, sound generated by wind farms can propagate distances of several tens of kilometers. This propagation is the result of various interacting factors: (1) stable atmospheric conditions in the atmospheric boundary layer at the wind-farm site create strong wind gradients that enhance the production of wind farm sound with TS characteristics, (2) the stable atmosphere also creates favorable conditions for the generation of sound waveguides in the lower troposphere that allow for propagation of sound, and (3) stable atmospheric conditions at the receiver imply lower atmospheric turbulence and lower atmospheric noise increasing detectability, especially for lower-frequency long-propagated signal that start merging into the background noise. We have described and characterized a source of infrasound signal that can propagate distances on the order of tens of kilometers and can be used to study changes in the lower troposphere and also can be used to test infrasound instrumentation such as different array topologies or spatial wind filters under continuously changing conditions.

Acknowledgments

Data for arrays LAG, MOT, and LISA are being submitted to IRIS-DMC (<http://ds.iris.edu/ds/nodes/dmc/>) under the experiment name and number: "Microbaroms" 201363, respectively. The raw waveforms from the SNL array are proprietary of Sandia National Laboratories and not publicly available; however, the results of the f-k analysis for this array can be retrieved from <https://github.com/omarmarcillo/SNL-array-f-k-results.git>. The radiosonde data are available at the repository of the Department of Atmospheric Science of the University of Wyoming (<http://weather.uwyo.edu/upperair/sounding.html>). We thank D. Baker and E. Morton for field deployments and R. Whitaker and Y.J. Kim for their comments on different aspects of this work, which helped to strengthen this paper. We thank also D. Beecher from the Environmental Department of Pueblo of Laguna for her support in the deployment of the LAG array. This research was funded by the Los Alamos Laboratory Directed Research and Development program. Sandia National Laboratories is a multiprogram laboratory managed and operated by Sandia Corporation, a wholly owned subsidiary of Lockheed Martin Corporation, for the U.S. Department of Energy's National Nuclear Security Administration under contract DE-AC04-94AL85000.

References

- Arturo Soriano, L., W. Yu, and J. D. J. Rubio (2013), Modeling and control of wind turbine, *Math. Probl. Eng.*, 2013, 982597, doi:10.1155/2013/982597.
- Assink (2012), Infrasound as upper atmospheric monitor, PhD thesis, Natl. Center for Physical Acoustics, Univ. of Mississippi, Miss.
- Baidya Roy, S., S. W. Pacala, and R. L. Walko (2004), Can large wind farms affect local meteorology?, *J. Geophys. Res.*, 109, D19101, doi:10.1029/2004JD004763.
- Clark, K., N. W. Miller, and J. J. Sanchez-Gasca (2010), Modeling of GE wind turbine-generators for grid studies, Tech. Rep. Version 3.4 B, 4. Sponsored by General Electric International, Inc.
- Diffendorfer, J. E., Compton, R., Kramer, L., Ancona, Z., and Norton, D. (2014), Onshore industrial wind turbine locations for the United States through July 2013, *U.S. Geol. Surv. Data Ser.*, 817.
- Doolan, C. J., D. J. Moreau, and L. A. And Brooks (2012), Wind turbine noise mechanisms and some concepts for its control, *Acoust. Aust.*, 40(1), 7–13.
- Drob, D. P., J. M. Picone, and M. Garcés (2003), Global morphology of infrasound propagation, *J. Geophys. Res.*, 108(D21), 4680, doi:10.1029/2002JD003307.
- Emeis, S. (2010), *Surface-Based Remote Sensing of the Atmospheric Boundary Layer*, Springer, Dordrecht, Netherlands.
- Fee, D., and M. Garcés (2007), Infrasonic tremor in the diffraction zone, *Geophys. Res. Lett.*, 34, L16826, doi:10.1029/2007GL030616.
- Garcés, M. A., R. A. Hansen, and K. G. Lindquist (1998), Traveltimes for infrasonic waves propagating in a stratified atmosphere, *Geophys. J. Int.*, 135(1), 255–263.
- Grosveld, F. W. (1985), Prediction of broadband noise from horizontal axis wind turbines, *J. Propul. Power*, 1(4), 292–299.
- Hau, E. (2013), *Wind Turbines: Fundamentals, Technologies, Application, Economics*, 3rd ed., Springer, Berlin.
- Herrin, E. T., T. S. Kim, and B. W. Stump (2006), Evidence for an infrasound waveguide, *Geophys. Res. Lett.*, 33, L07815, doi:10.1029/2005GL025491.
- Hubbard, H. H., and Shepherd, K. P. (1990), Wind turbine acoustics, Rep. 3057, Sponsored by National Aeronautics and Space Administration, Office of Management, Scientific and Technical Information Division.
- Hubbard, H. H., and K. P. Shepherd (1991), Aeroacoustics of large wind turbines, *J. Acoust. Soc. Am.*, 89(6), 2495–2508.
- Jensen, F. B., W. A. Kuperman, M. B. Porter, and H. Schmidt (2011), *Computational Ocean Acoustics*, 2nd ed., pp. 1–794, AIP Press, Springer, New York.
- Johansson, L. (2003), Sound propagation around off-shore wind turbines, Licentiate Thesis, Dep. of Civil and Architectural Engineering, Kth, Stockholm, Sweden.

- Jung, S. S., W.-S. Cheung, C. Cheong, and S.-H. Shin (2008), Experimental identification of acoustic emission characteristics of large wind turbines with emphasis on infrasound and low-frequency noise, *J. Korean Phys. Soc.*, *53*(4), 1897–1905.
- Keith, D. W., J. F. Decarolis, D. C. Denkenberger, D. H. Lenschow, S. L. Malyshev, S. Pacala, and P. J. Rasch (2004), The influence of large-scale wind power on global climate, *Proc. Natl. Acad. Sci. U.S.A.*, *101*(46), 16,115–16,120.
- Kirk-Davidoff, D. B., and D. W. Keith (2008), On the climate impact of surface roughness anomalies, *J. Atmos. Sci.*, *65*(7), 2215–2234.
- Larsson, C., and O. Ohlund (2014), Amplitude modulation of sound from wind turbines under various meteorological conditions, *J. Acoust. Soc. Am.*, *135*(1), 67–73.
- Møller, H., and C. S. Pedersen (2011), Low-frequency noise from large wind turbines, *J. Acoust. Soc. Am.*, *129*(6), 3727–3744.
- Moriarty, P., and P. G. Migliore (2003), *Semi-Empirical Aeroacoustic Noise Prediction Code for Wind Turbines*, Natl. Renewable Energy Lab., Golden, Colo.
- Muljadi, E., and C. P. Butterfield (2001), Pitch-controlled variable-speed wind turbine generation, industry applications, *IEEE Trans.*, *37*(1), 240–246.
- NCPA (2012), *Ncpaprop, Computer Software*, Natl. Center for Physical Acoustics, Oxford, Miss.
- Nehorai, A., and B. Porat (1986), Adaptive comb filtering for harmonic signal enhancement, acoustics, speech and signal processing, *IEEE Trans.*, *34*(5), 1124–1138.
- Nishi, K., and S. Ando (1998), An optimal comb filter for time-varying harmonics extraction, *leice Trans. Fundam. A*, *81*(8), 1622–1627.
- Oerlemans, S., and J. G. Schepers (2009), Prediction of wind turbine noise and validation against experiment, *Int. J. Aeroacoust.*, *8*(6), 555–584.
- Oerlemans, S., P. Sijtsma, and B. Méndez López (2007), Location and quantification of noise sources on a wind turbine, *J. Sound Vib.*, *299*(4–5), 869–883.
- Ohlund, O., and C. Larsson (2015), Meteorological effects on wind turbine sound propagation, *Appl. Acoust.*, *89*, 34–41.
- O’neal, R. D., R. D. Hellweg, and R. M. Lampeter (2011), Low frequency noise and infrasound from wind turbines, *Noise Control Eng. J.*, *59*(2), 135–157.
- Pennock, K. (2012), Updated Eastern Interconnect wind power output and forecasts for ERGIS, Rep. Nrel/Sr-5500-56616. 1–17 p. Sponsored by Natl. Renewable Energy Lab.
- Porté-Agel, F., H. Lu, and Y.-T. Wu (2014), Interaction between large wind farms and the atmospheric boundary layer, *Procedia Iutam*, *10*, 307–318.
- Salomons, E. M. (2001), *Computational Atmospheric Acoustics*, 1st ed., pp. 1–335, Springer, Dordrecht, Netherlands.
- Schlichting, H., and K. Gersten (2000), *Boundary-Layer Theory*, 8th ed., pp. 1–800, Springer, Berlin.
- Schweitzer, J., J. Fyen, S. Mykkeltveit, and T. Kvaerna (2002), Seismic arrays, in *IASPEI New Manual of Seismological Observatory Practice*, pp. 1–51, Geoforschungszentrum, Potsdam, Germany.
- Son, E., H. Kim, H. Kim, W. Choi, and S. Lee (2010), Integrated numerical method for the prediction of wind turbine noise and the long range propagation, *Curr. Appl. Phys.*, *10*, S316–S319.
- Talmadge, C. L., R. Waxler, X. Di, K. E. Gilbert, and S. Kulichkov (2008), Observation of low-frequency acoustic surface waves in the nocturnal boundary layer, *J. Acoust. Soc. Am.*, *124*(4), 1956–1962.
- Thomas, C. (2008), Array signal processing, in *Handbook of Signal Processing in Acoustics*, pp. 1655–1665, Springer, New York.
- Van Den Berg, G. (2005), The beat is getting stronger: The effect of atmospheric stability on low frequency modulated sound of wind turbines, *Noise Notes*, *4*(4), 15–40.
- Van Den Berg, G. P. (2004), Effects of the wind profile at night on wind turbine sound, *J. Sound Vib.*, *277*(4–5), 955–970.
- Waxler, R., K. E. Gilbert, and C. Talmadge (2008), A theoretical treatment of the long range propagation of impulsive signals under strongly ducted nocturnal conditions, *J. Acoust. Soc. Am.*, *124*(5), 2742–2754.
- Willshire Jr, W. L. (1985), Long range downwind propagation of low-frequency sound, Rep. 86409, pp. 1–21, Sponsored by Natl. Aeronautics and Space Administration.
- Wolf, A., T. Lutz, W. Würz, E. Krämer, O. Stalnov, and A. Seifert (2014), Trailing edge noise reduction of wind turbine blades by active flow control, *Wind Energy*, *18*(5), 909–923.